Chapter 11

Accuracy Investigation of De-Embedding Techniques Based on Electromagnetic Simulation for On-Wafer RF Measurements

Takuichi Hirano, Kenichi Okada, Jiro Hirokawa and Makoto Ando

Additional information is available at the end of the chapter

http://dx.doi.org/10.5772/48431

1. Introduction

Millimeter-wave CMOS RF circuits have received substantial attention in recent years, motivated by advances in CMOS processing. Figure 1 shows on-wafer measurement using probes, which is commonly used in research and development of RF front-end circuits. De-embedding is necessary to remove the effect of pads in on-wafer measurements of RF circuits. Thru-Reflect-Line (TRL) calibration technique [1][2][3] and the de-embedding technique using open and short patterns [4] have been used conventionally. The authors applied the Thru-Line (TL) de-embedding technique [5] to remove the effect of pads from the measured S-parameters of RF circuits on a Si CMOS substrate. The TL de-embedding technique requires two patterns (Thru and Line) while the TRL de-embedding requires three patterns (Thru, Reflect and Line). The TL de-embedding technique can characterize left and right pads under the assumption that left and right pads have the same characteristics while TRL de-embedding cannot characterize pads, without knowing characteristic impedance of the line used for example. Other de-embedding methods, such as double delay [6], through-only [7], and multi line (or L-2L) de-embedding [8][9], have been proposed. However, these all use approximation of pads, or parasitic component, by an equivalent circuit model while the TL de-embedding method treats pads rigorously with S-parameters. The effectiveness of TL de-embedding has been investigated in [10].

It is very difficult to keep repeatability of measurement in such high frequencies over millimeter-wave band. Hence, the electromagnetic (EM) simulation technology becomes important. This paper explains EM simulation modeling for on-wafer measurement using a GSG probe. By utilizing the result of EM simulation, the accuracy of de-embedding techniques (open-short, TRL, and TL) are compared and discussed.

The chapter is organized as follows. Section 2 describes structure of pads and transmission line considered in the chapter. Section 3 presents open-short, TRL and TL de-embedding techniques. Section 4 presents EM simulation modeling for on-wafer measurement using a GSG probe. The gap between ground (G) and signal (S) pads is excited by a lumped source. Section 5 discusses the accuracy of de-embedding techniques (open-short, TRL, and TL). The accuracy degradation of open-short de-embedding technique is quantitatively investigated via numerical simulation, which is verified in section 4.

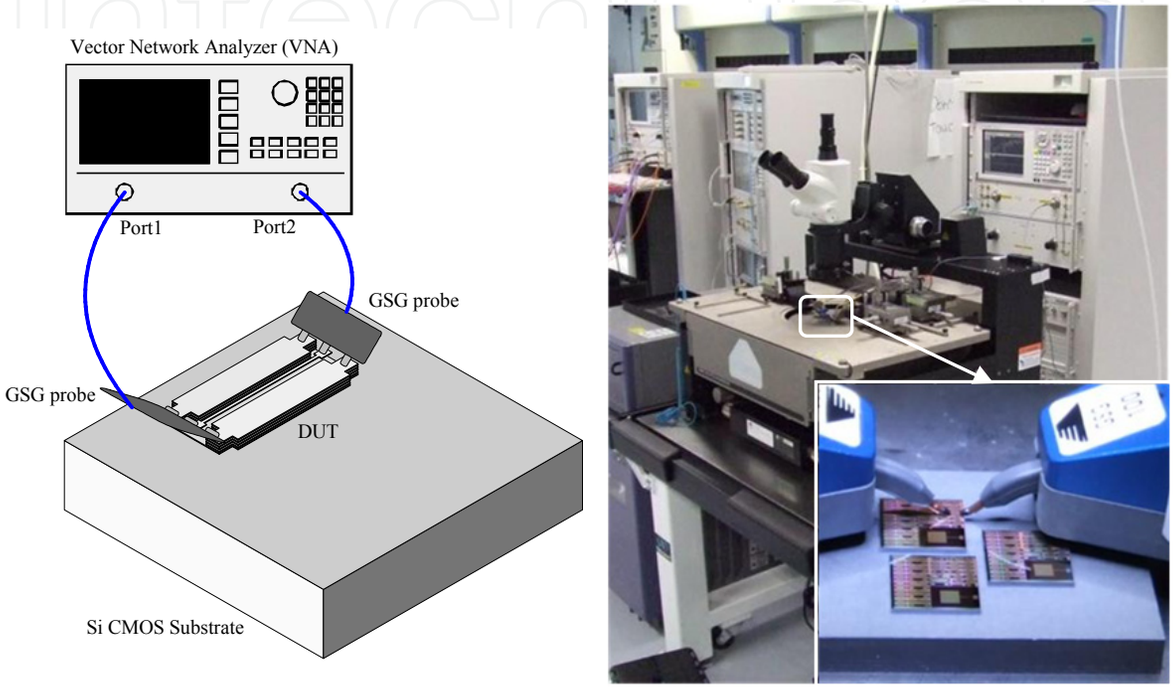

(a) Conceptual block diagram (b) Photograph of equipments

Figure 1. On-wafer measurement using probes.

2. Structure of pads and transmission line

The structure of pads and transmission lines are shown in Figure 2. The GSG pad is used for touching with the GSG probe. A guided microstrip line (G-MSL) on a Si CMOS substrate [11], which has metal walls on both sides of the signal line, is used as the transmission line between the GSG pads as shown in Figure 2. The G-MSL with dummy metal fills is shown in Figure 3. The transmission line consists of several metal (Aluminum) layers and vias which connect them. SiO_2 is used as an insulator between the metal layers. The ground plane and signal line are realized by the bottom and top metal layers, respectively. The width and thickness of the signal line are 10 μm and 1 μm, respectively. The characteristic impedance is designed to be about 50 Ohm. There are metal walls, or guides, on both sides of the signal line which consists of the metal layers and vias [11]. The role of the guide is to increase the metal density to satisfy design rules and to suppress unwanted leakage at corners. The distance from the guide walls to the edges of the signal line is 20 μm to ensure that the guide does not affect transmission characteristic of the microstrip mode.

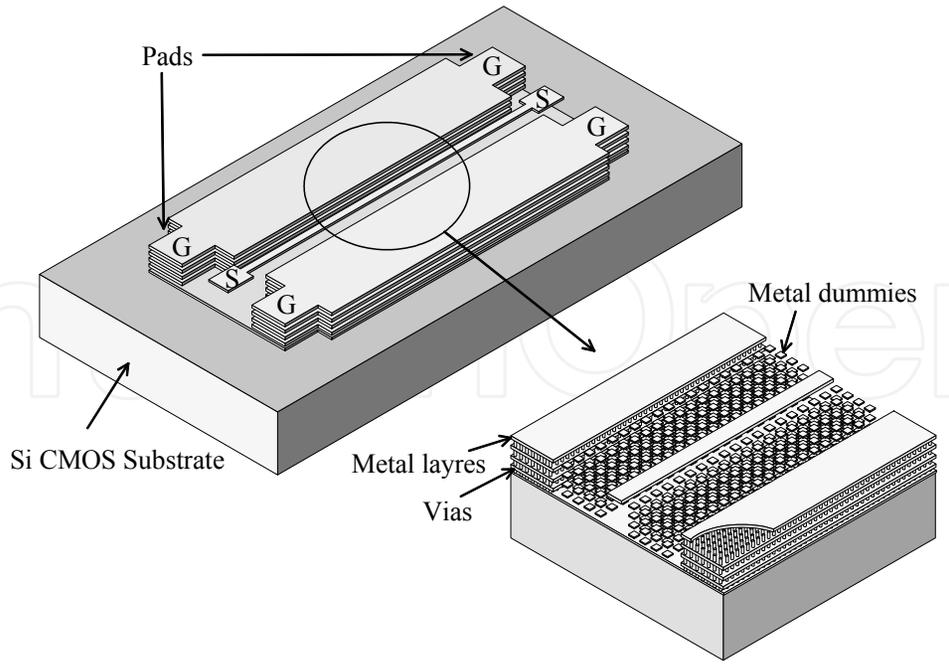

Figure 2. Structures of pads and guided microstrip line (G-MSL).

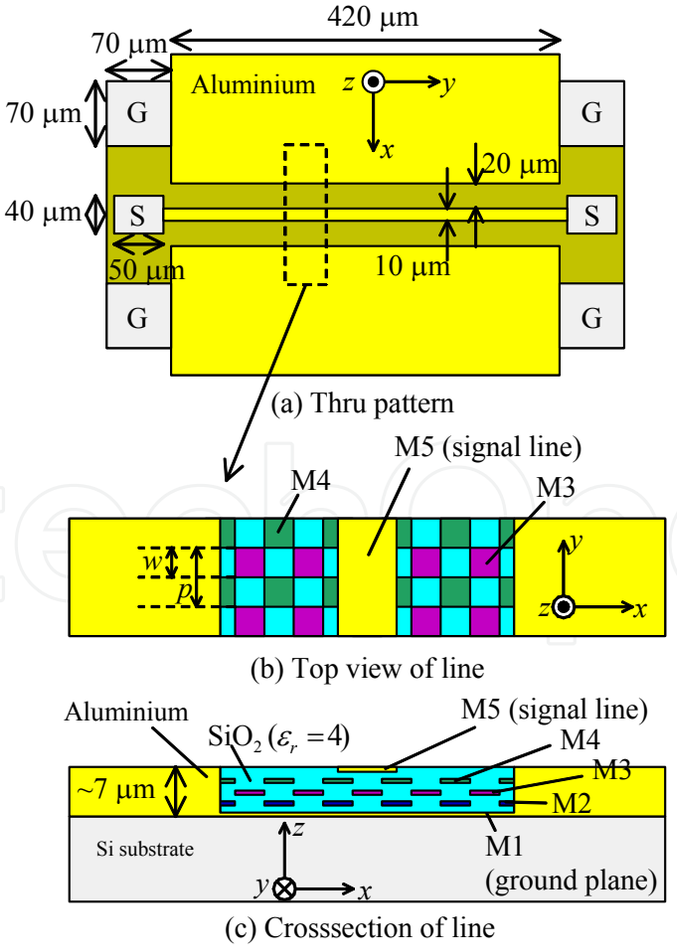

Figure 3. Thru pattern and structure of a guided microstrip line.

3. De-embedding techniques

Algorithms of open-short, TRL and TL de-embedding techniques are introduced in this section. Table 1 shows the patterns used in each de-embedding method.

Pattern		Method		
		TRL	TL	Open/Short
Thru	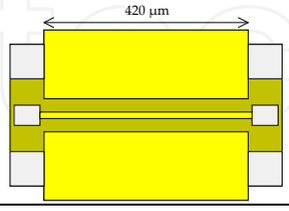	✓	✓	
Reflect (~Open)	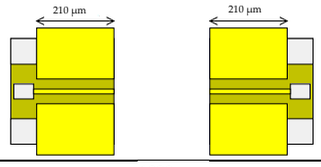	✓		✓
Line	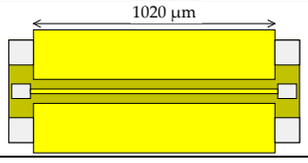	✓	✓	
Short	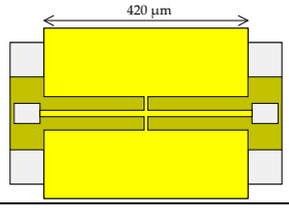			✓

Table 1. Pattern used in de-embedding methods

3.1. De-embedding techniques using open-short patterns

The open-short de-embedding technique [4] is reviewed and outlined here. In the open-short de-embedding technique, the parasitic component of pads is approximated by the equivalent circuit topology shown in Figure 4.

i) Three measurements are made to obtain the transmission line characteristics shown in Figure 4(i). The first measurement is done for the open-pattern, resulting in the open two-port Y-parameters $Y^{(\text{open})}$. The second measurement is done for the short-pattern, resulting in the short two-port Y-parameters $Y^{(\text{short})}$. The third measurement is done for a thru-pattern, which includes the GSG pads at both ends of a short line, described by the two-port Y-parameters $Y^{(\text{SUT})}$. The thru-pattern can be replaced by an arbitrary structure with the GSG pads, which is named the structure under test (SUT).

(ii) The thru-pattern is approximated by the equivalent circuit topology shown in Figure 4(ii). Parasitic elements Y_{p1}, Y_{p2} and Y_{p3} can be determined from $Y^{(\text{open})}$ by comparing with π -circuit parameters.

$$Y^{(\text{open})} = \begin{bmatrix} Y_{11}^{(open)} & Y_{12}^{(open)} \\ Y_{21}^{(open)} & Y_{22}^{(open)} \end{bmatrix} = \begin{bmatrix} Y_{p1} + Y_{p3} & -Y_{p3} \\ -Y_{p3} & Y_{p2} + Y_{p3} \end{bmatrix} \tag{1}$$

By comparing matrix elements, Y_{p1}, Y_{p2} and Y_{p3} can be determined.

$$\begin{cases} Y_{p1} = Y_{11}^{(open)} + Y_{12}^{(open)} \\ Y_{p2} = Y_{22}^{(open)} + Y_{12}^{(open)} \\ Y_{p3} = -Y_{12}^{(open)} \end{cases} \tag{2}$$

(iii) Parasitic elements Y_{p1}, Y_{p2} and Y_{p3} can be removed from $Y^{(\text{short})}$; $Y^T = Y^{(\text{short})} - Y^{(\text{open})}$. Parasitic elements Z_{s1}, Z_{s2} and Z_{s3} can be determined by comparing with T-circuit parameters after transforming Y^T into Z-parameters Z^T.

$$Z^T = \begin{bmatrix} Z_{11}^T & Z_{12}^T \\ Z_{21}^T & Z_{22}^T \end{bmatrix} = \begin{bmatrix} Z_{s1} + Z_{s3} & Z_{s3} \\ Z_{s3} & Z_{s2} + Z_{s3} \end{bmatrix} \tag{3}$$

By comparing matrix elements, Z_{s1}, Z_{s2} and Z_{s3} can be determined.

$$\begin{cases} Z_{s1} = Z_{11}^T - Z_{12}^T \\ Z_{s2} = Z_{22}^T - Z_{12}^T \\ Z_{s3} = Z_{12}^T \end{cases} \tag{4}$$

(iv) The Y-parameters for thru, only transmission line characteristic, $Y^{(\text{DUT})}$ can be obtained by removing Y_{p1}, Y_{p2}, Y_{p3}, Z_{s1}, Z_{s2} and Z_{s3}. Parasitic elements Y_{p1}, Y_{p2} and Y_{p3} can be removed by subtracting $Y^{(\text{open})}$ from $Y^{(\text{SUT})}$. Parasitic elements Z_{s1}, Z_{s2} can be removed with the fundamental matrix (F-matrix). Finally, Z_{s3} can be removed with the Z-matrix.

It is noted that a lumped element can be the DUT although the transmission line is assumed as the DUT in this paper. De-embedding technique using electromagnetic (EM) simulator [12], with higher accuracy than the open/short de-embedding technique, is also proposed when the DUT is a lumped element.

3.2. De-embedding techniques using Thru-Reflect-Line patterns

The Thru-Reflect-Line (TRL) calibration technique [1][2][3], which is widely used for network analyzer calibration, can be used for deembedding of pads directly.

3.3. De-embedding techniques using Thru-Line patterns

The Thru-Line (TL) de-embedding technique [5] uses Thru (T) and Line (L) patterns, which have different lengths as shown in Figure 5. The line pattern is longer (by ΔL) than the Thru

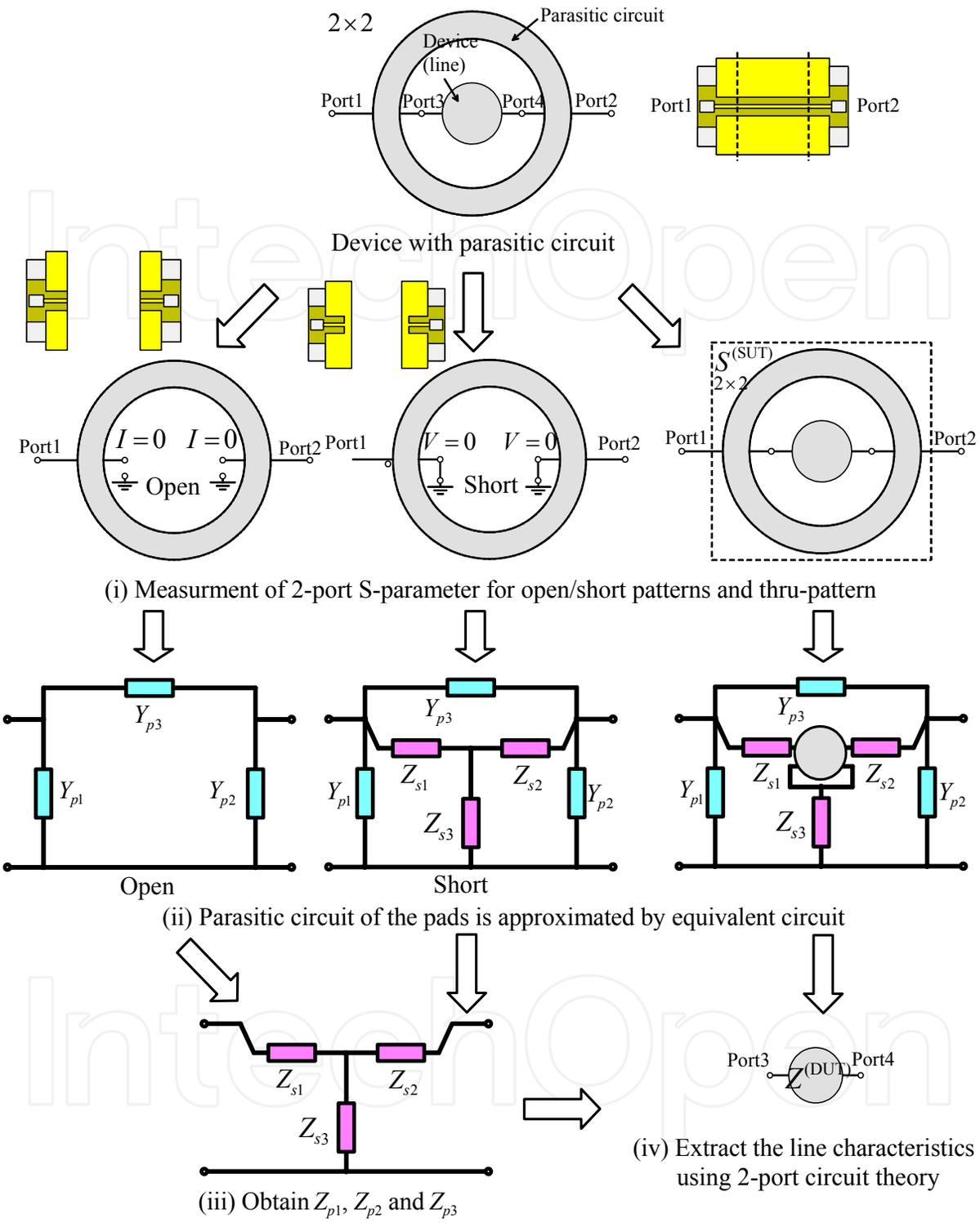

Figure 4. De-embedding technique using open and short patterns.

pattern. The overall characteristics of the Line pattern can be decomposed as a cascade connection of pads and line parts as shown in Figure 6. The assumption that two pads have completely same characteristics is necessary in TL de-embedding. From Figure 6, the total characteristics of Thru and Line patterns are

$$\begin{cases} \rho_t = S_{11} + \dfrac{{S_{12}}^2 S_{22}}{1-{S_{22}}^2} \\ \tau_t = \dfrac{{S_{12}}^2}{1-{S_{22}}^2} \end{cases} \qquad \begin{cases} \rho_l = S_{11} + \dfrac{{S_{12}}^2 S_{22}\Gamma^2}{1-{S_{22}}^2\Gamma^2} \\ \tau_l = \dfrac{{S_{12}}^2\Gamma}{1-{S_{22}}^2\Gamma^2} \end{cases} \tag{5}$$

where ρ_t and τ_t are the reflection and transmission coefficients of the Thru pattern; ρ_l and τ_l are the reflection and transmission coefficients of the Line pattern; and S_{11}, $S_{12}(=S_{21})$, and S_{22} are the S-parameters of the pads. Here, ρ_t, τ_t, ρ_l, and τ_l can be measured while $S_{11}, S_{22}, {S_{12}}^2$, and $\Gamma(=e^{-\gamma\Delta L})$ are unknowns. With the four equations in (5), these unknowns can be found by solving the non-linear equations, for example by using Mathematica [13].

$$\begin{cases} S_{11} = \dfrac{{\rho_l}^2 - {\rho_t}^2 - {\tau_l}^2 + {\tau_t}^2 \pm A}{2(\rho_l - \rho_t)} \\ S_{22} = \dfrac{{\rho_l}^2 - 2\rho_l\rho_t + {\rho_t}^2 - {\tau_l}^2 + {\tau_t}^2 \pm A}{2(-\rho_l + \rho_t)\tau_t} \\ {S_{12}}^2 = -\dfrac{1}{2\tau_t}\{(\rho_l - \rho_t)^2 - 2{\tau_t}^2 \pm B \\ \qquad -\dfrac{1}{(\rho_l - \rho_t)^2}(2{\rho_l}^2{\tau_l}^2 - 4\rho_l\rho_t{\tau_l}^2 + 2{\rho_t}^2{\tau_l}^2 \\ \qquad + (\tau_l - \tau_t)(\tau_l + \tau_t)(-({\tau_l}^2 - {\tau_t}^2) \pm B))\} \\ \Gamma = \dfrac{-{\rho_l}^2 + 2\rho_l\rho_t - {\rho_t}^2 + {\tau_l}^2 + {\tau_t}^2 \pm A}{2\tau_l\tau_t} \end{cases} \tag{6}$$

where

$$\begin{aligned} A &= \sqrt{-4(\rho_l - \rho_t)^2{\tau_t}^2 + \left\{(\rho_l - \rho_t)^2 - {\tau_l}^2 + {\tau_t}^2\right\}^2} \\ B &= \sqrt{(\rho_l - \rho_t - \tau_l - \tau_t)(\rho_l - \rho_t + \tau_l - \tau_t)(\rho_l - \rho_t - \tau_l + \tau_t)(\rho_l - \rho_t + \tau_l + \tau_t)} \end{aligned} \tag{7}$$

It must be noted that there are two sets of solutions to (6) indicated by the double sign. The propagation constant can be calculated from Γ.

$$\gamma = -\frac{\ln\Gamma}{\Delta L} \tag{8}$$

Selecting the correct solution from the two sets of solutions in (6) and (7) is uncomplicated. If the transmission line is a right-handed waveguide, the phase constant is positive, and a set of solutions which gives a positive phase constant $\beta = \mathrm{Im}[\gamma]$ is chosen at the lowest considered frequency near direct current (DC). At the next higher frequency point, in frequency sweeping, a set of solutions is chosen so that the phase constant is near the previous lower frequency point.

The effect of the pads can be de-embedded from a structure under test (SUT) by the following procedure:

(i) Measure the S-matrix of the SUT $S^{(\mathrm{SUT})}$.

(ii) Transform $S^{(\mathrm{SUT})}$ into a cascade matrix (T-matrix) $T^{(\mathrm{SUT})}$. Now $T^{(\mathrm{SUT})}$ is implied to be $T^{(\mathrm{SUT})} = T^{(\mathrm{PAD\text{-}L})} T^{(DUT)} T^{(\mathrm{PAD\text{-}R})}$, where $T^{(\mathrm{PAD\text{-}L})}$, $T^{(\mathrm{PAD\text{-}R})}$ and $T^{(DUT)}$ are the T-matrixes of the left pad, right pad, and device under test (DUT) embedded in the pads, respectively. The $T^{(\mathrm{PAD\text{-}L})}$ and $T^{(\mathrm{PAD\text{-}R})}$ values can be calculated from $S^{(\mathrm{PAD\text{-}L})}$ and $S^{(\mathrm{PAD\text{-}R})}$, with the elements obtained in (6) (See also Figure 6).

(iii) $T^{(DUT)}$ can be obtained by matrix operations: $T^{(DUT)} = \left(T^{(\mathrm{PAD\text{-}L})}\right)^{-1} T^{(\mathrm{SUT})} \left(T^{(\mathrm{PAD\text{-}R})}\right)^{-1}$. Finally, $S^{(\mathrm{DUT})}$ is obtained by transformation from $T^{(DUT)}$, and de-embedding of the pads can be performed.

A sample Mathematica source code is given in Appendix.

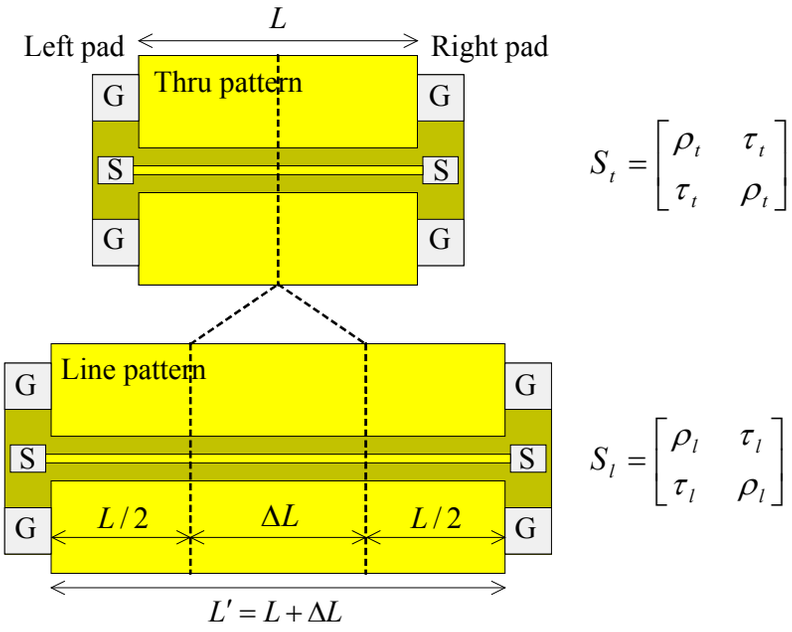

Figure 5. Thru and line patterns.

4. Electromagnetic modeling

This section verifies the modeling and accuracy of the electromagnetic (EM) simulator. The FEM-based EM simulator, Ansoft HFSS Ver.11 [14], was used for EM analysis in the chapter.

4.1. Symmetric pattern

Figure 7 shows the model for the analysis of the thru-pattern in HFSS. Due to the symmetry of the structure and excitation, the model for the analysis of the Figure 3 thru-pattern can be reduced to half of the whole structure, as suggested in Figure 7. A magnetic wall, or perfect magnetic conductor (PMC), is assumed at the center of symmetry. The absorbing boundary, or radiation boundary in HFSS, conditions are applied to the other outer boundary walls. The gap between ground (G) and signal (S) pads is excited by a lumped source. Lumped

ports with 100 Ohm intrinsic impedances, which is double of probe impedance because of image theory, were used for the excitations.

To verify the accuracy of the EM simulation, the calculated value is compared with the measured one. A micrograph of a fabricated chip is shown in Figure 8. The chip is 2.5 mm square and an 0.18 μm CMOS process is used. In the measurements, 100 μm-pitch GSG probes were used, and the system was calibrated using the impedance standard substrate (ISS). Smith charts of the S-parameters for the thru, line, and reflect patterns are shown in Figures 9, 10, and 11, respectively. The calculated and measured results agreed very well for all three patterns.

Then, sensitivity of lumped port position and size is investigated. Figure 12 shows position and size of lumped port in the GSG pad. Reflection coefficient S_{11} and transmission coefficient S_{12} (=S_{21}) are shown in Figure 13 and Figure 14, respectively, with various sets of width (w), left pad offset (d_l) and right pad offset (d_r) (both offsets are prescribed in a similar manner). w is varied from 10 μm to 30 μm. d_l and d_r are varied from -15 μm to 15 μm. It is found that there are no significant differences in results. These results suggest that the probe positioning error is not serious in measurement. Results indicated by "edge1" and "edge2" are obtained with the excitation model in which lumped port is arranged at the edge of the GSG pad as shown in Figure 15. w_a in Figure 15 is 20 μm for "edge1" while it is 50 μm for "edge2". The phase of S_{11} begins to show different value in high frequency region. The result indicated by "vertical" is obtained with the excitation model in Figure 16. The phase of S_{12} begins to show different value in high frequency region. However, the results of these excitation models show good agreement.

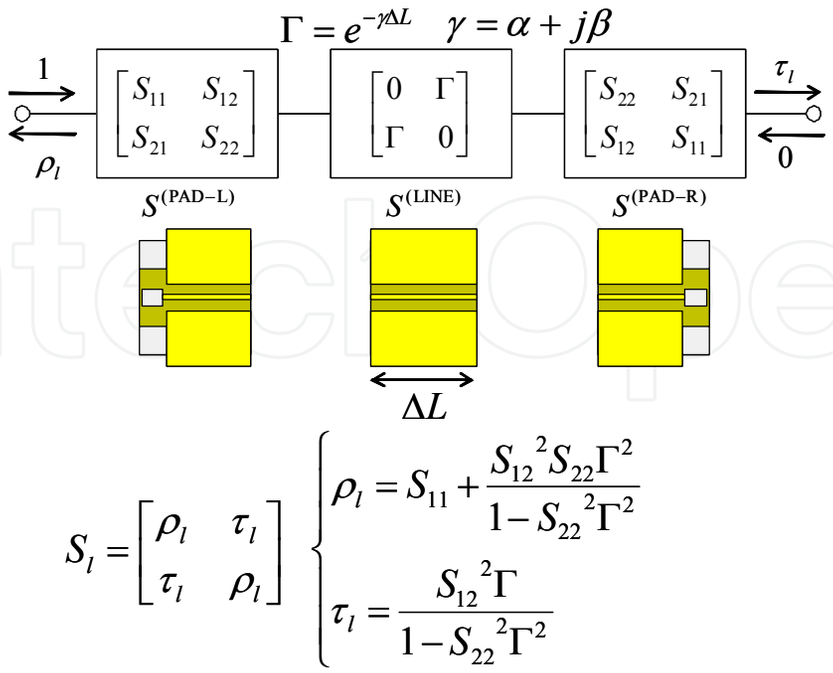

Figure 6. Cascading expression of the line pattern.

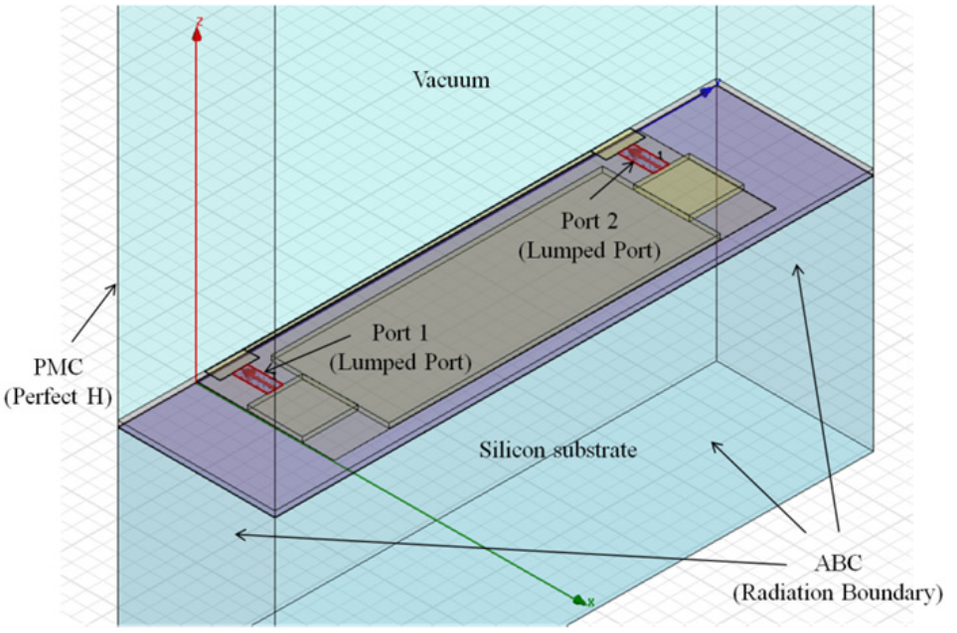

(a) Bird's eye view

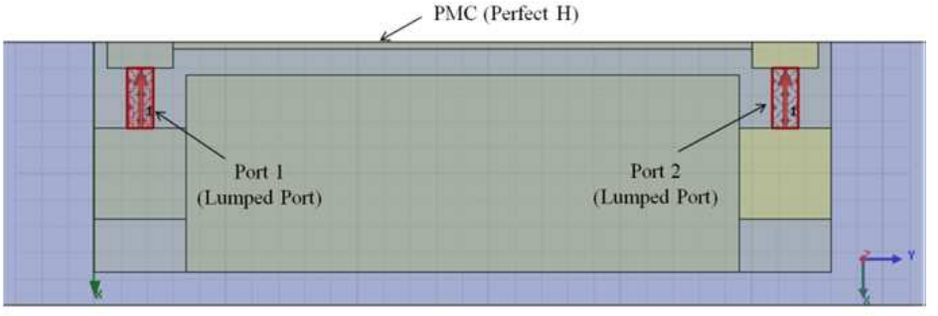

(b) Top view

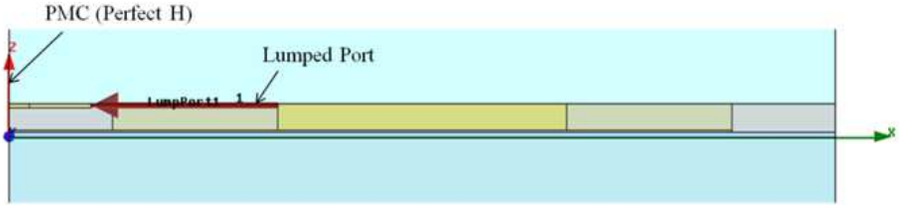

(c) Cross-sectional view

Figure 7. Analysis model of thru-pattern in HFSS.

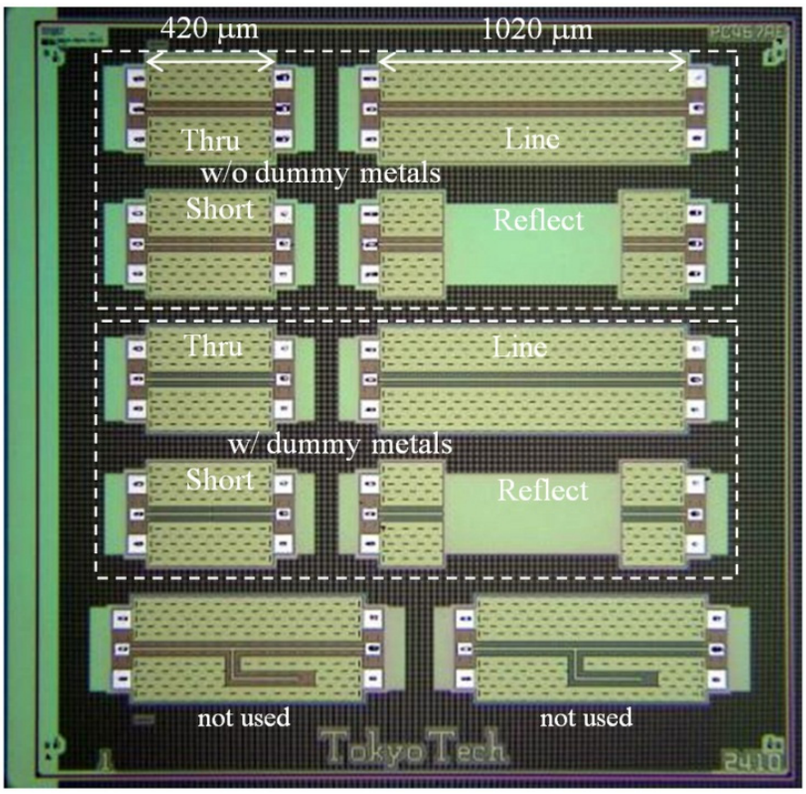

Figure 8. Chip photo (process: CMOS 0.18μm, chip size: 2.5 mm x 2.5 mm)

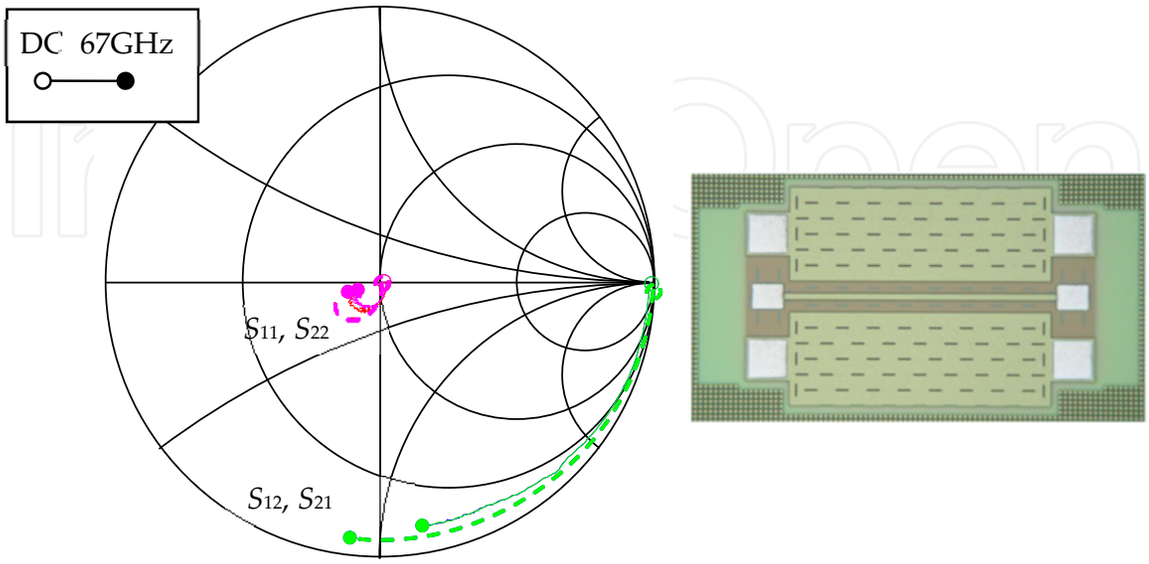

Figure 9. Smith chart of thru-pattern. (Solid line: measurements, broken line: simulation)

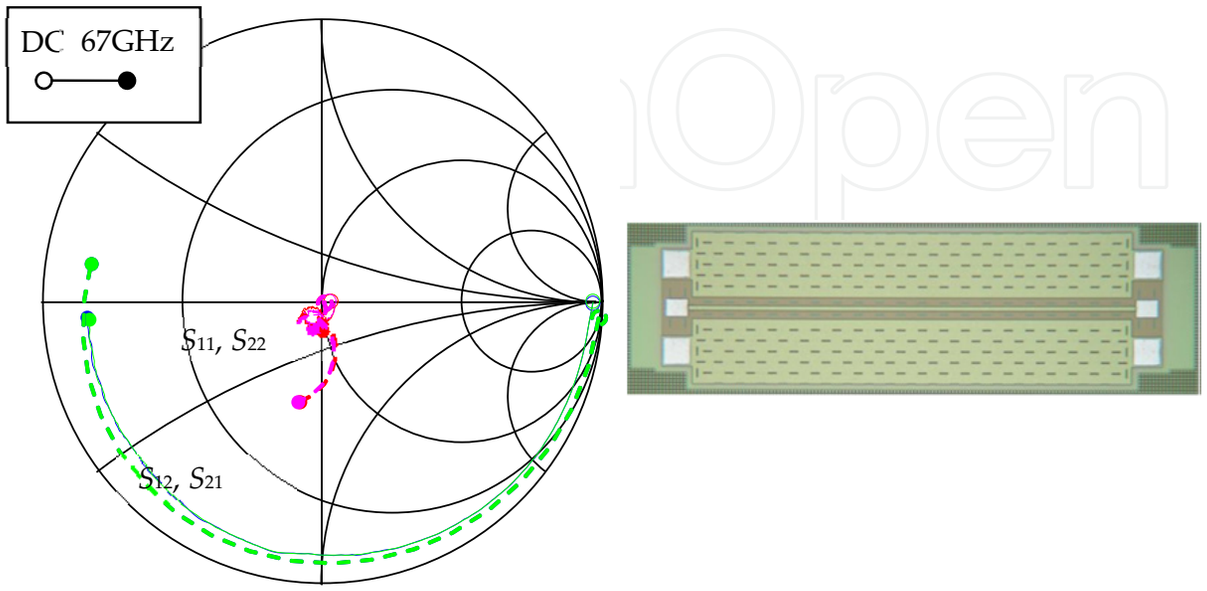

Figure 10. Smith chart of line-pattern in HFSS.

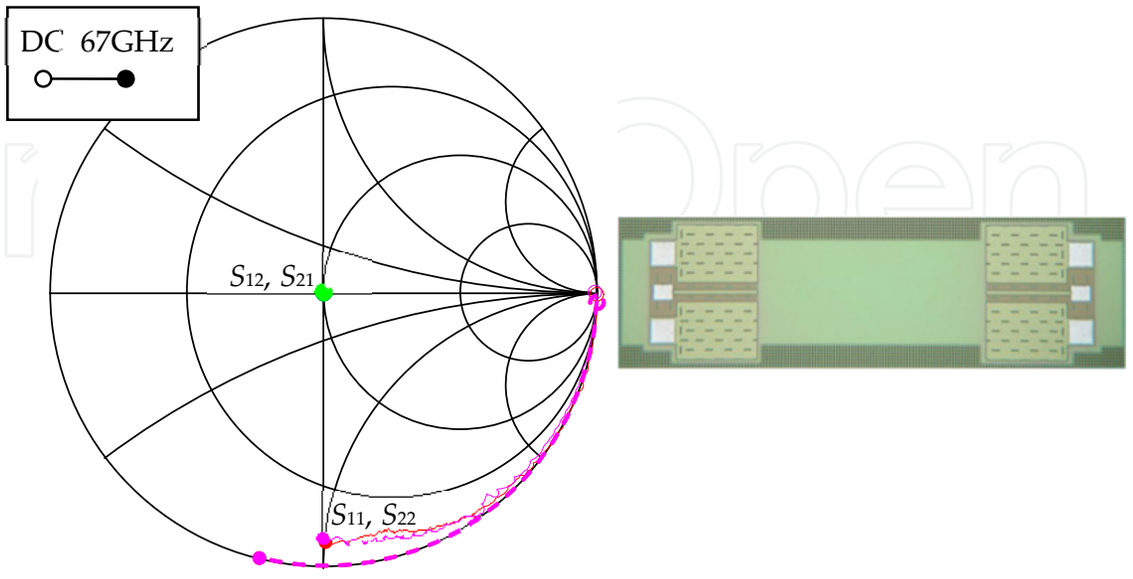

Figure 11. Smith chart of reflect-pattern in HFSS.

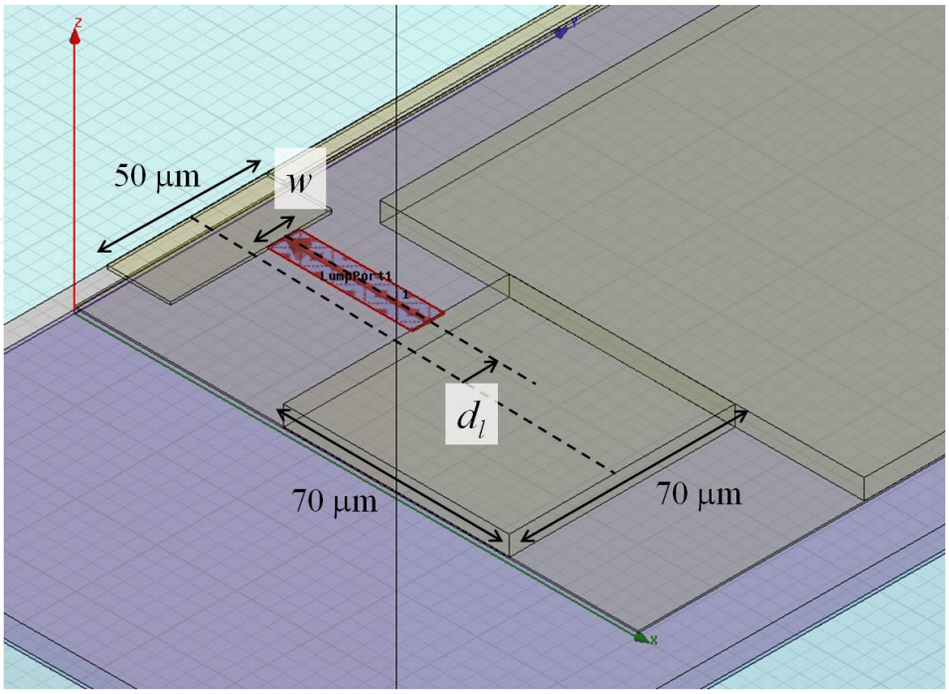

Figure 12. Position and size of lumped port in the GSG pad.

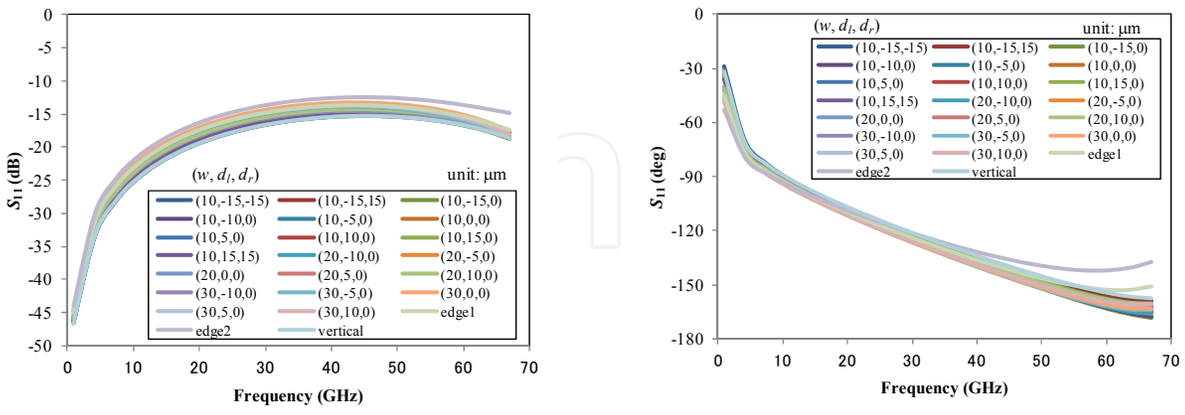

(a) Amplitude (b) Phase

Figure 13. Position sensitivity of lumped port for S_{11} of thru-pattern.

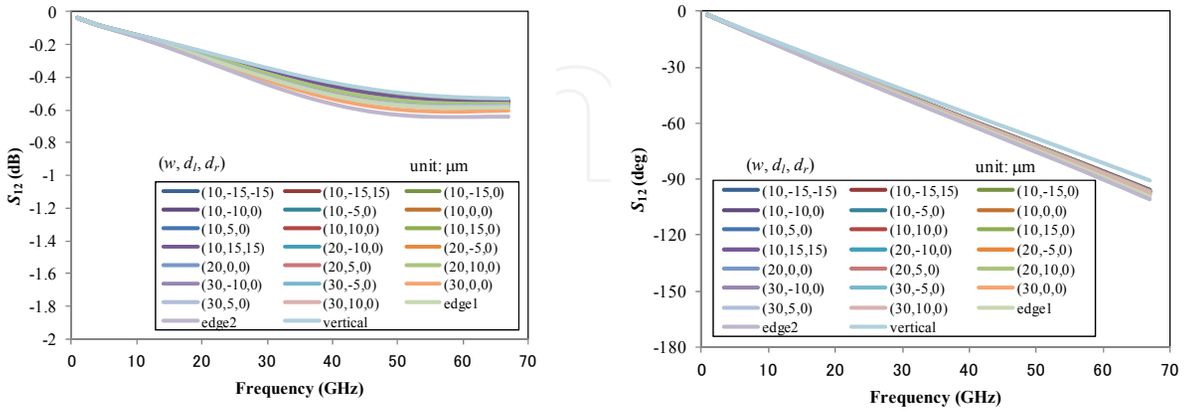

(a) Amplitude (b) Phase

Figure 14. Position sensitivity of lumped port for S_{12} of thru-pattern.

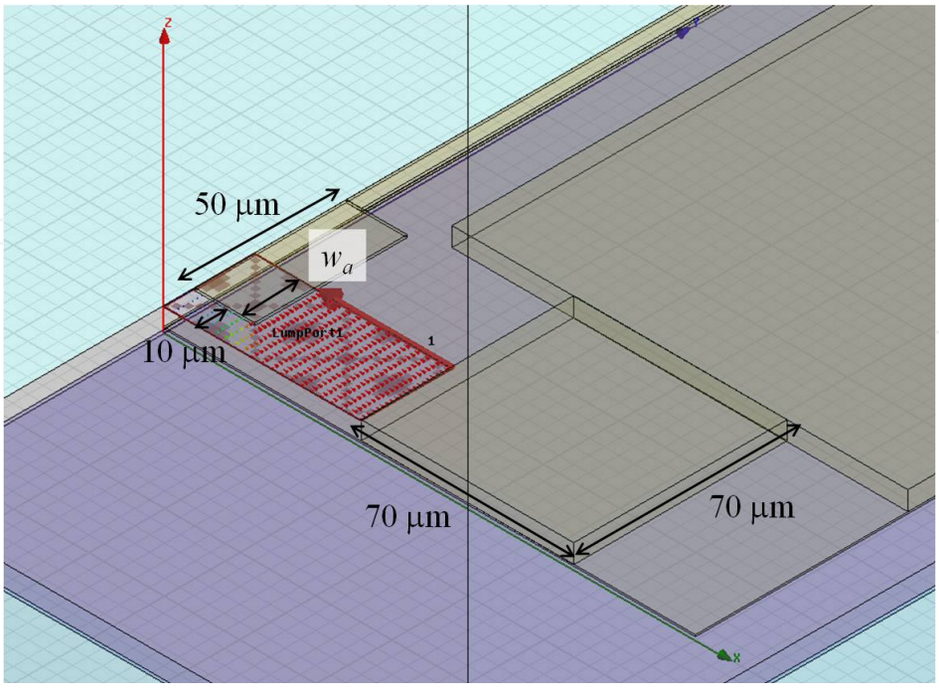

Figure 15. Lumped port arranged at the edge of the GSG pad.

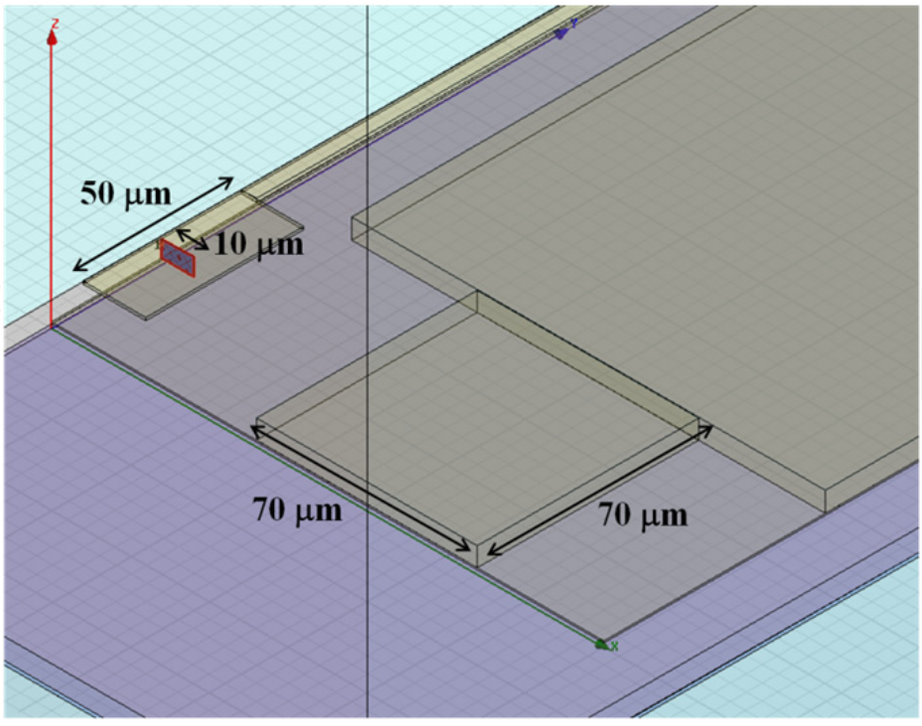

Figure 16. Lumped port arranged vertically in the GSG pad.

4.2. Asymmetric pattern

In this section, excitation modeling is extended in order to treat more general problem. Figure 17 shows EM excitation-modeling for GSG pad include asymmetric pattern while symmetric pattern is considered in the previous section. Port 1, 2, 3 and 4 have 100 Ohm intrinsic impedance when the impedance of the GSG probe is 50 Ohm. The objective of the following discussion is to convert 4×4 S-matrix obtained by simulation into 2×2 S-matrix to compare with VNA measurement. S-matrix for the Figure 17 is written as

$$\begin{bmatrix} b_1 \\ b_2 \\ \hdashline b_3 \\ b_4 \end{bmatrix} = \left[\begin{array}{cc:cc} S_{11} & S_{12} & S_{13} & S_{14} \\ S_{21} & S_{22} & S_{23} & S_{24} \\ \hdashline S_{31} & S_{32} & S_{33} & S_{34} \\ S_{41} & S_{42} & S_{43} & S_{44} \end{array}\right] \begin{bmatrix} a_1 \\ a_2 \\ \hdashline a_3 \\ a_4 \end{bmatrix}. \tag{9}$$

Port 1 and Port 2 are identically excited ($a_1 = a_2 = a_1'$), and Port 3 and Port 4 are also identically excited ($a_3 = a_4 = a_2'$). The GSG pad is symmetric and coming waves to Port 1 and Port 2 are identical ($b_1 = b_2 = b_1'$) because they are guided by the G-MSL. This is same for Port 3 and Port 4 ($b_3 = b_4 = b_2'$).

$$\begin{bmatrix} b_1' \\ b_1' \\ \hdashline b_2' \\ b_2' \end{bmatrix} = \left[\begin{array}{cc:cc} S_{11} & S_{12} & S_{13} & S_{14} \\ S_{21} & S_{22} & S_{23} & S_{24} \\ \hdashline S_{31} & S_{32} & S_{33} & S_{34} \\ S_{41} & S_{42} & S_{43} & S_{44} \end{array}\right] \begin{bmatrix} a_1' \\ a_1' \\ \hdashline a_2' \\ a_2' \end{bmatrix} \tag{10}$$

$$\begin{cases} b_1' = (S_{11} + S_{12})a_1' + (S_{13} + S_{14})a_2' \\ b_1' = (S_{21} + S_{22})a_1' + (S_{23} + S_{24})a_2' \\ b_2' = (S_{31} + S_{32})a_1' + (S_{33} + S_{34})a_2' \\ b_2' = (S_{41} + S_{42})a_1' + (S_{43} + S_{44})a_2' \end{cases} \tag{11}$$

Because of the symmetry of the GSG pad, $S_{11} = S_{22}$, $S_{12} = S_{21}$, $S_{13} = S_{14} = S_{23} = S_{24}$, $S_{31} = S_{32} = S_{41} = S_{42}$, $S_{33} = S_{44}$, $S_{34} = S_{43}$ holds. The first and second equations in (11) are identical. Also, the third and fourth equations in (11) are identical. As a result, the following 2×2 S-matrix is obtained.

$$\begin{bmatrix} S_{11}' & S_{12}' \\ S_{21}' & S_{22}' \end{bmatrix} = \begin{bmatrix} S_{11} + S_{12} & S_{13} + S_{14} \\ S_{31} + S_{32} & S_{33} + S_{34} \end{bmatrix} \tag{12}$$

If only one GSG probe is used to measure reflection, the reflection coefficient can be obtained by

$$\Gamma = \frac{b}{a} = S_{11} + S_{12} = S_{21} + S_{22}. \tag{13}$$

To verify the formulation of (12), the EM excitation-modeling for thru-pattern shown in Figure 18 is compared with the modeling shown in Figure 7. Figure 19 shows the frequency characteristic of reflection and transmission coefficient for the thru-pattern. The result indicated by "Cal" is obtained by the model in Figure 7, and the result indicated by "Cal (4-ports to 2-ports)" is obtained by the model in Figure 18. They agreed very well each other. Figure 19 shows two short-circuited lines, which have asymmetric structure as an example. Figure 20 shows the frequency characteristic of S-parameters for the structure shown in Figure 19. Calculated results agreed very well with measured results, and (12) is validated.

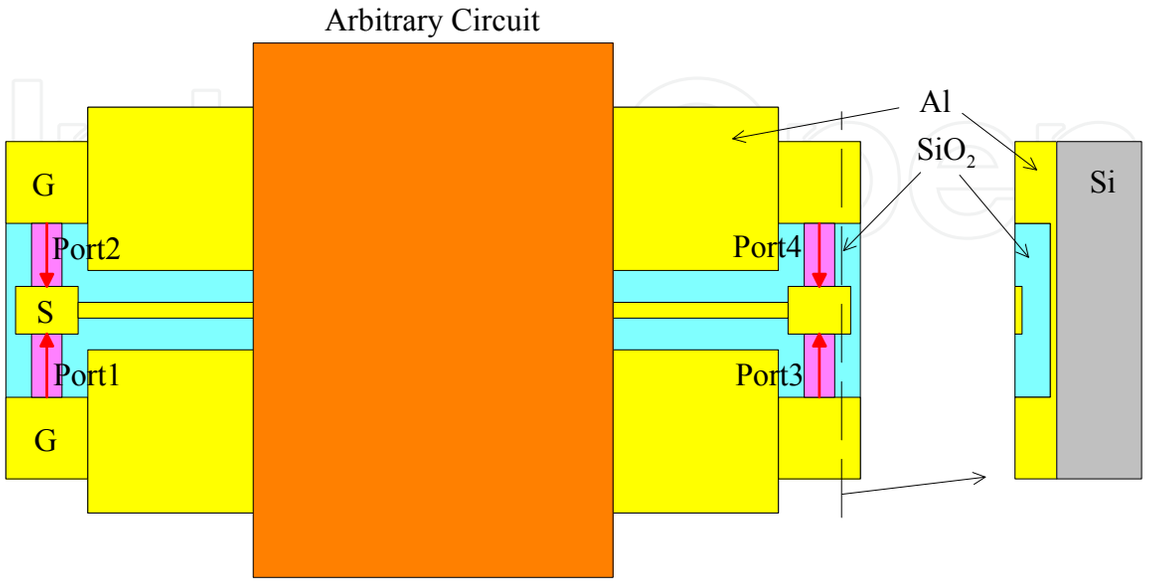

Figure 17. EM excitation-modeling for GSG pad include asymmetric pattern.

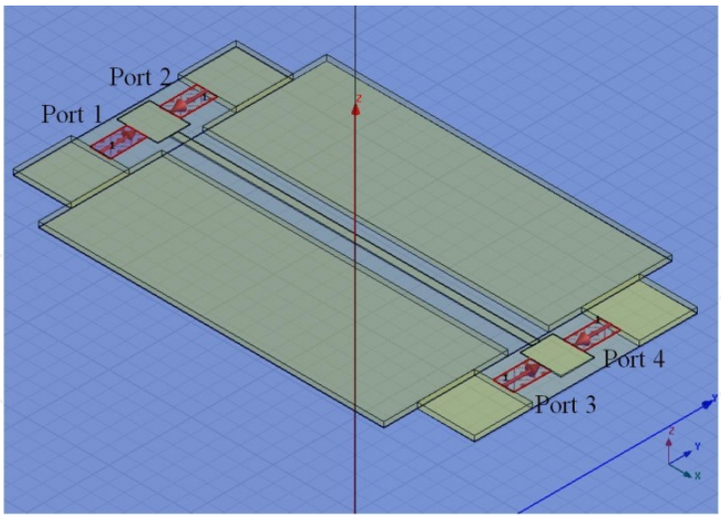

Figure 18. Four port excitation model for thru-pattern.

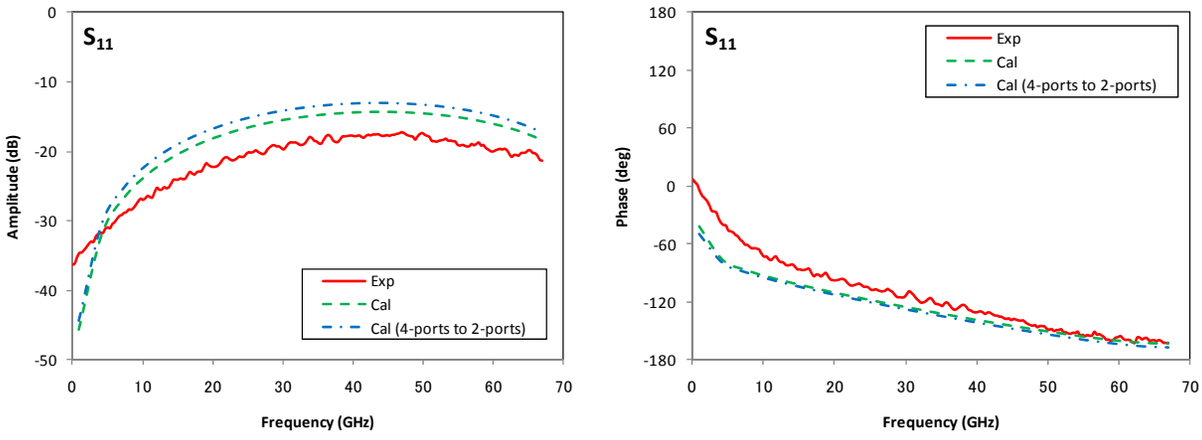

(a) Reflection coefficient S_{11}

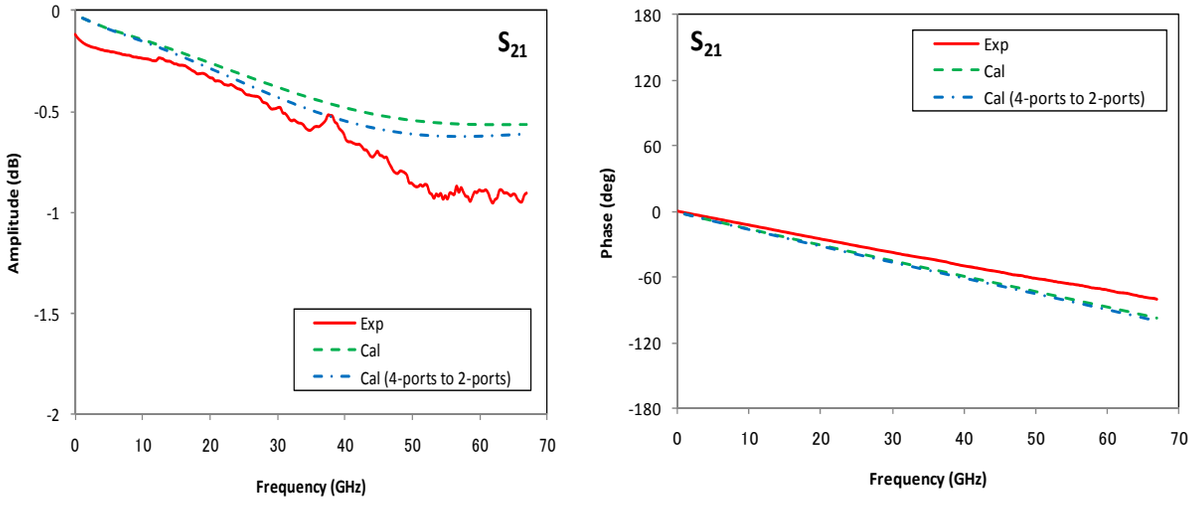

(b) Transmission coefficient S_{21}

Figure 19. Comparison between two-port and four-port excitation model for thru-pattern.

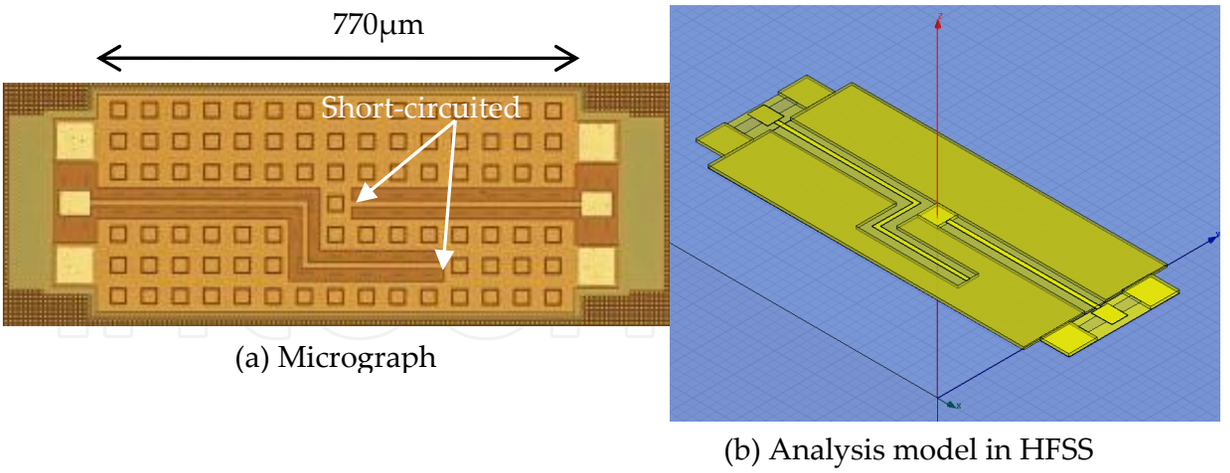

Figure 20. Two short-circuited lines.

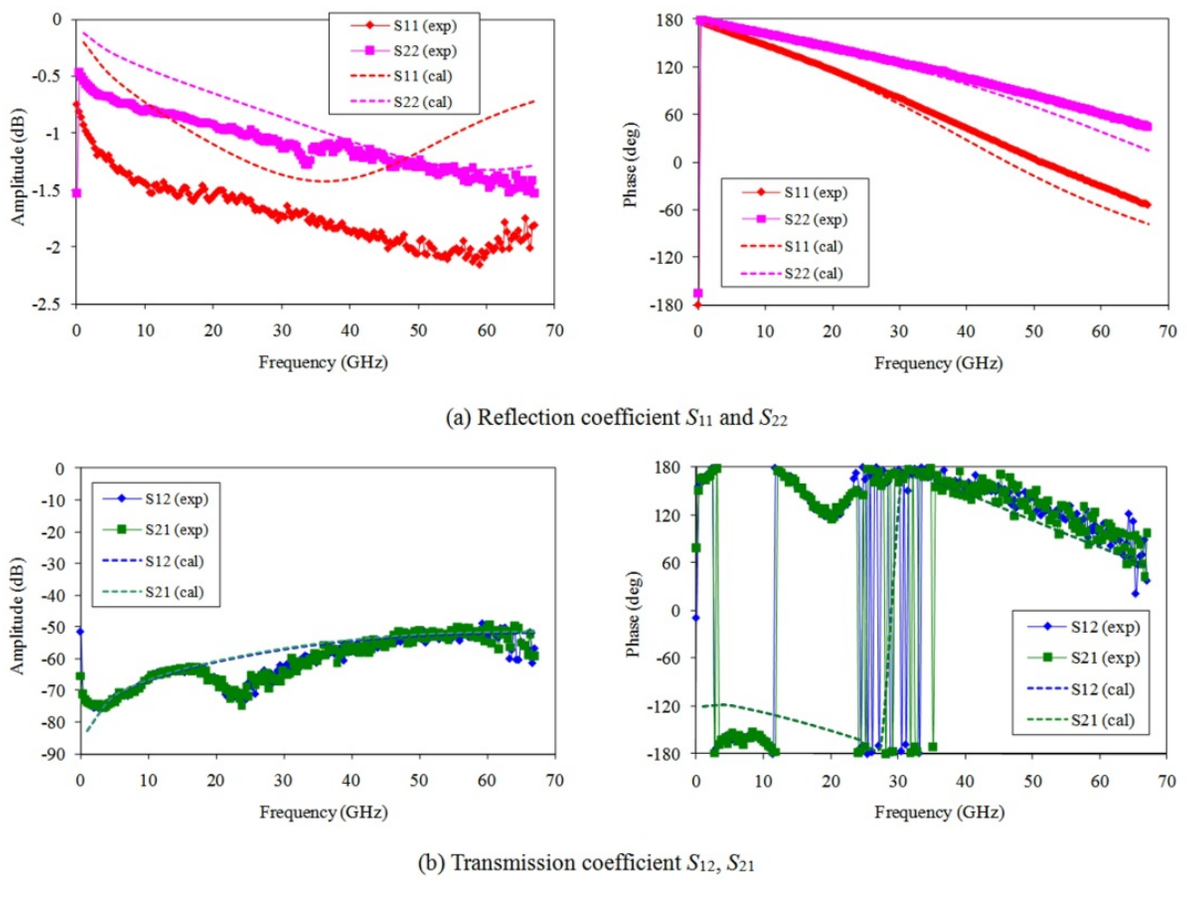

Figure 21. Frequency characteristic of S-parameters for two short-circuited lines shown in Figure 20.

5. Results

5.1. Comparison of accuracy between de-embedding techniques

The frequency characteristic of the propagation constant for the G-MSL is extracted by de-embedding techniques, and shown in Figure 22. The solid and broken lines represent results without and with dummy metal fills (5 m square; w=5 m and p=10 m in Figure 3) in the G-MSL, respectively. The loss of the G-MSL with dummy metal fills is slightly larger than that without dummy metal fills. The phase constant of the G-MSL with dummy metal fills is slightly larger than that without dummy metal fills because the dummy metal fills result in an effect like an artificial dielectric compound. The line with "Cal." is the calculated result with the method in [15]. The measured results agreed well with the calculations. Figure 22 shows that the accuracy of TL de-embedding technique is as good as that of the TRL de-embedding technique.

Figure 23 shows the characteristic impedance of the transmission lines. The characteristic impedance was obtained from the ratio of the voltage V to the current I. The voltage V is calculated by the tangential line integral of the electric field from the ground plane to the signal line. One half of the current $I/2$ is calculated by the tangential line integral of the magnetic field around the signal line. The characteristic impedance is obtained using the de-embedding technique [16] together with a characterization of the pads using the TL de-embedding technique. Very good agreement between the calculated and measured results was obtained. As the frequency increases, the real part of the characteristic impedance approaches 50 Ohm and the imaginary part of the characteristic impedance approaches 0 Ohm.

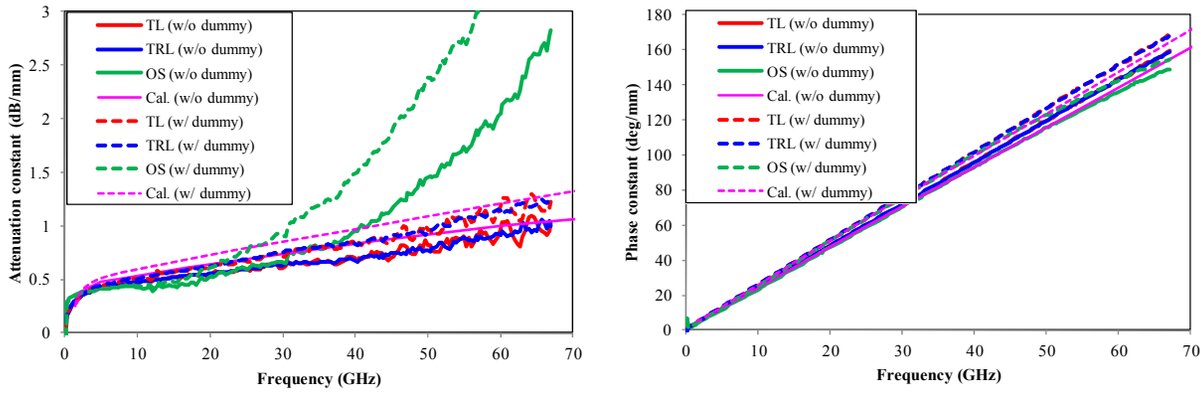

(a) Attenuation constant

(b) Phase constant

Figure 22. Extracted propagation constant of the G-MSL.

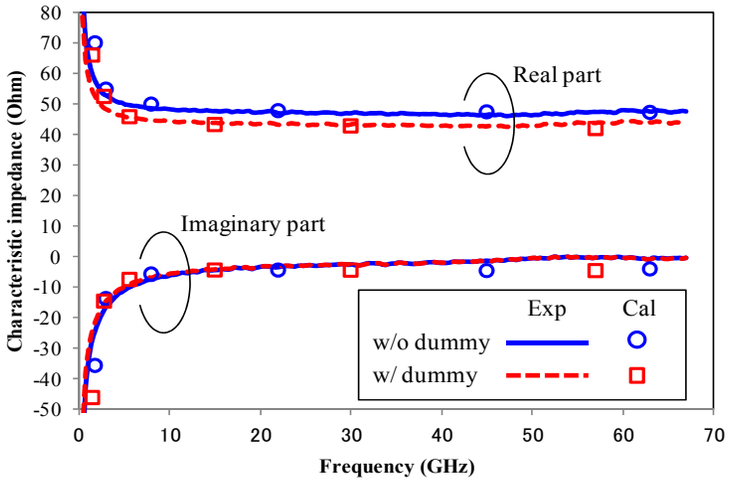

Figure 23. Extracted Characteristic impedance of the G-MSL.

5.2. Accuracy investigation of open/short de-embedding technique

The accuracy of de-embedding methods using thru-line patterns, thru-reflect-line patterns and open/short patterns will be discussed numerically in this section. Open and short patterns used in the simulation are shown Figure 24. The lengths from left and right pads to the open or short ends are $l/2$. Figure 25 shows the transmission coefficient S_{21} for the G-MSL with the length of 600 μm extracted by each method. The line with "3-D FEM (HFSS)" is the result directly obtained by the S_{21} of the 3-D FEM analysis using wave port excitation in HFSS. The line with "2-D FEM (HFSS)" is the result obtained using the propagation constant analyzed by the port solution by the 2-D FEM analysis in HFSS. These must be identical, and the differences are negligible. The results with "TRL", "TL", and "OS" are obtained after de-embedding the influence of the pads and using the TRL, TL, and open/short de-embedding techniques, respectively. Except for the "OS" they agreed very well with the results of the "3-D FEM (HFSS)," and the effectiveness of the TL and TRL de-embedding methods is verified. The accuracy of the open/short de-embedding method becomes poorer as the frequency increases. This is because the pads cannot be approximated well by an equivalent circuit in the high frequency band [12]. The accuracy of the ''OS'' can be improved if patterns with shorter lengths are used [17]. The accuracy of the TL de-embedding method is as good as that of TRL de-embedding method, allowing the conclusion that the accuracy of the TL de-embedding method is validated.

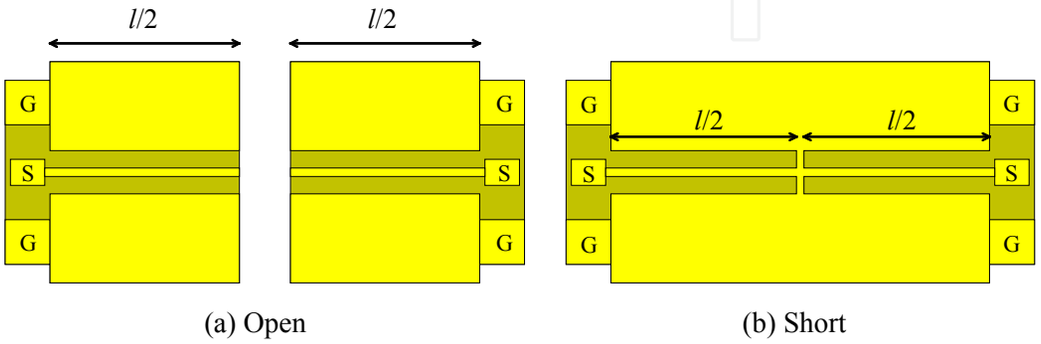

Figure 24. Extracted Characteristic impedance of the G-MSL.

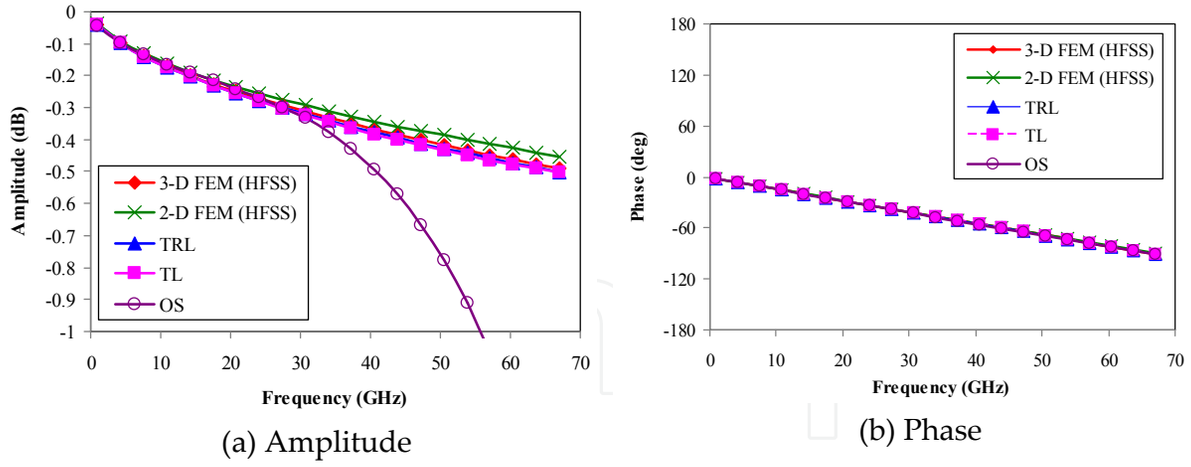

(a) Amplitude (b) Phase

Figure 25. Extracted transmission coefficient S_{21} of the 600 μm-length G-MSL (l=420 μm in Figure 24).

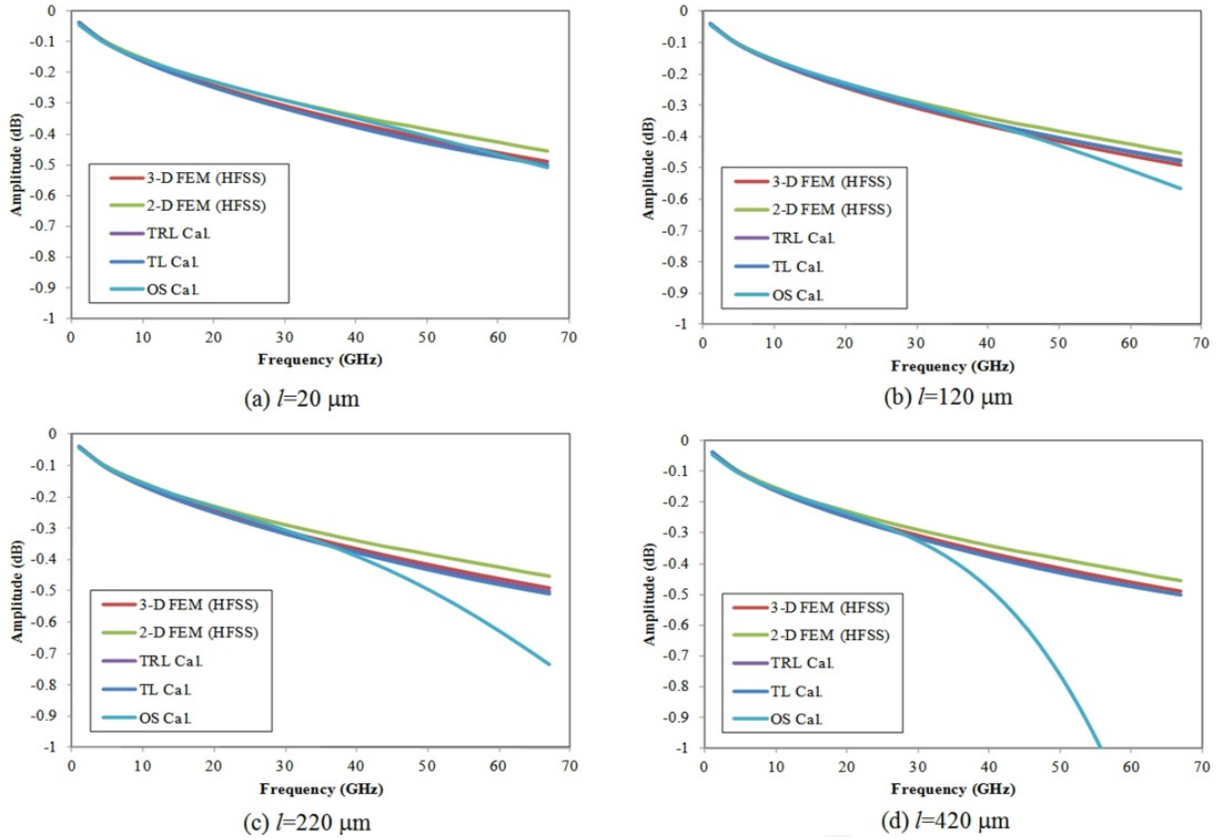

(a) l=20 μm (b) l=120 μm

(c) l=220 μm (d) l=420 μm

Figure 26. Extracted transmission coefficient S_{21} of the 600 μm-length G-MSL for several length of open/short patterns.

To investigate the accuracy of the open-short de-embedding technique, numerical simulation was performed to extract S_{21} of a G-MSL with 600 μm-length. Figure 26 shows extracted S_{21} for the 600 μm-length G-MSL using calibration patterns with l=20 μm, 120 μm, 220 μm, 420 μm, respectively. A line of "3-D FEM (HFSS)" is the result obtained by S_{21} of the 3-D FEM analysis for the 600 μm-length G-MSL. The result indicated by "2-D FEM (HFSS)" is port analysis solution. Results indicated by "TRL", "TL" and "OS" are obtained after

applying TRL, TL, and open-short de-embedding techniques, respectively. Results are obtained by simulation using HFSS. The accuracy of the TRL and TL de-embedding techniques is very good while that of open-short de-embedding technique differs in high frequency. The accuracy becomes higher as the length l of the open and short patterns becomes shorter. Figure 27 shows the error of the extracted S_{21} defined by

$$error \equiv \left| \frac{S_{21}^{\text{true}} - S_{21}^{\text{extracted}}}{S_{21}^{\text{true}}} \right|. \tag{14}$$

The result indicated by "3-D FEM (HFSS)" is used for S_{21}^{true}. The error becomes larger when the length of the open and short pattern becomes longer.

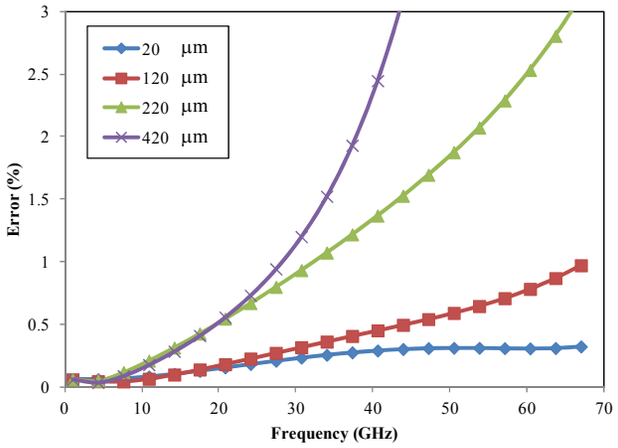

Figure 27. Error of the extracted transmission coefficient S_{21} of the 600 μm-length G-MSL with open-short de-embedding technique.

6. Conclusion

In this paper, EM simulation modeling for on-wafer measurement using a GSG probe was presented. The gap between ground (G) and signal (S) pads is excited by a lumped source. Transformation formula from 4-port to 2-port S-matrix expression was derived. The accuracy of EM simulation was verified by comparing with measurements. Results of EM simulation by changing excitation model suggest that the probe positioning error is not serious in measurement.

TL de-embedding technique was applied for on-wafer measurement using a GSG probe. The accuracy of de-embedding techniques (open-short, TRL, and TL) were compared and discussed. It was found that the accuracy of TRL and TL de-embedding technique is approximately the same. Degradation of accuracy in open-short de-embedding technique was quantitatively investigated via numerical simulation. In the open-short de-embedding technique, the accuracy becomes higher as the lengths of the open and short patterns become shorter.

Author details

Takuichi Hirano, Kenichi Okada, Jiro Hirokawa and Makoto Ando
Tokyo Institute of Technology, Japan

Acknowledgement

This work was supported in part by Semiconductor Technology Academic Research Center (STARC). The chip in this study has been fabricated in the chip fabrication program of the VLSI Design and Education Center (VDEC), the University of Tokyo in collaboration with Rohm Corporation and Toppan Printing Corporation. The authors would like to express their deepest gratitude to Toshihiko Mori of FUJITSU, Osamu Kobayashi of STARC, Naoko Ono of TOSHIBA, Toshiakira Ando of STARC/PANASONIC, and Ryuichi Fujimoto of STARC /TOSHIBA for their fruitful discussion.

Appendix

Example Mathematica [13] code is shown here.

```
In[1]:= sol = Solve[{ρl == s11 + s12sq * s22 * Γ^2 / (1 - s22^2 * Γ^2), zl == s12sq * Γ / (1 - s22^2 * Γ^2),
      ρt == s11 + s12sq * s22 / (1 - s22^2), zt == s12sq / (1 - s22^2)},
     {s11, s12sq, s22, Γ}] // Simplify;
s11A[ρl_, zl_, ρt_, zt_] = s11 /. sol[[1]];
s12sqA[ρl_, zl_, ρt_, zt_] = s12sq /. sol[[1]];
s22A[ρl_, zl_, ρt_, zt_] = s22 /. sol[[1]];
ΓA[ρl_, zl_, ρt_, zt_] = Γ /. sol[[1]];

s11B[ρl_, zl_, ρt_, zt_] = s11 /. sol[[2]];
s12sqB[ρl_, zl_, ρs_, zs_] = s12sq /. sol[[2]];
s22B[ρl_, zl_, ρt_, zt_] = s22 /. sol[[2]];
ΓB[ρl_, zl_, ρt_, zt_] = Γ /. sol[[2]];

(* Choose one of two solution sets *)
s11[ρl_, zl_, ρt_, zt_] := s11A[ρl, zl, ρt, zt];
s12sq[ρl_, zl_, ρt_, zt_] := s12sqA[ρl, zl, ρt, zt];
s22[ρl_, zl_, ρt_, zt_] := s22A[ρl, zl, ρt, zt];
Γ[ρl_, zl_, ρt_, zt_] := ΓA[ρl, zl, ρt, zt];

In[14]:= (* Formulas *)
TransStoT[s_] := 1/s[[2, 1]] * {{-Det[s], s[[1, 1]]}, {-s[[2, 2]], 1}};
TransTtoS[t_] := 1/t[[2, 2]] * {{t[[1, 2]], Det[t]}, {1, -t[[2, 1]]}};
```

In[16]:=
```
(* Thru-Line (TL) De-embedding *)
l1 = 420.0 * 10^-6; l2 = 1020.0 * 10^-6; dl = l2 - l1; dlScale = 0. * 10^-6;

(* Thru *)
smt = {{1. * 10^-16, 1.}, {1., 1. * 10^-16}}; (* Read measured data *)
tmt = TransStoT[smt];
(* Line *)
sml = {{2. * 10^-16, Exp[I * 1]}, {Exp[-I * 1], 2. * 10^-16}}; (* Read measured data *)
tml = TransStoT[sml];
(* Device to be extracted *)
smd = {{1., 2.}, {3., 4.}}; (* Read measured data *)
tmd = TransStoT[smd];

(* Thru *)
ρt = smt[[1, 1]];
τt = smt[[1, 2]];
(* Line *)
ρl = sml[[1, 1]];
τl = sml[[1, 2]];
```

In[27]:=
```
sal = {{1.0 * 10^-16, Γ[ρl, τl, ρt, τt]}, {Γ[ρl, τl, ρt, τt], 1.0 * 10^-16}};

spadL = {{s11[ρl, τl, ρt, τt], Sqrt[s12sq[ρl, τl, ρt, τt]]}, {Sqrt[s12sq[ρl, τl, ρt, τt]], s22[ρl, τl, ρt, τt]}};
tpadL = TransStoT[spadL];
spadR = {{s22[ρl, τl, ρt, τt], Sqrt[s12sq[ρl, τl, ρt, τt]]}, {Sqrt[s12sq[ρl, τl, ρt, τt]], s11[ρl, τl, ρt, τt]}};
tpadR = TransStoT[spadR];

γ = -Log[Γ[ρl, τl, ρt, τt]] / dl;
sdlScale = {{1. * 10^-16, Exp[-γ * dlScale]}, {Exp[-γ * dlScale], 1. * 10^-16}};
tdlScale = TransStoT[sdlScale];
tpadL = tpadL.tdlScale;
tpadR = tdlScale.tpadR;

tal = Inverse[tpadL].tml.Inverse[tpadR];
sal = TransTtoS[tal];

tad = Inverse[tpadL].tmd.Inverse[tpadR];
sad = TransTtoS[tad];
```

```
Check (identical to smd?)

In[41]:= TransTtoS[tpadL.tad.tpadR] // Chop

Out[41]= {{1., 2.}, {3., 4.}}
```

7. References

[1] G.F. Engen and C.A. Hoer, "'Thru-Reflect-Line': an improved technique for calibrating the dual six-port automatic network analyzer," IEEE Trans. Microwave Theory Tech., vol.MTT-27, No.12, Dec. 1979.

[2] P. Colestock and M. Foley, "A generalized TRL Algorithm for S-parameter de-embedding," Fermi National Accelerator Laboratory Technical Memo, TM-1781, April 1993.

[3] D. Rytting, IEEE MTT/ED seminar on Calibration and Error Correction Techniques for Network Analysis, OGI Center for Professional Development, September, 2004.

[4] M.C.A.M. Koolen, J.A.M. Geelen, and M.P.J.G. Versleijen, "An improved de-embedding technique for on-wafer high-frequency characterization," Proc. IEEE, Bipolar/BiCMOS Circuits and Tech. Meeting, pp.188-191, Sept. 1991.

[5] S. Georgakopoulos and S. Ogurtsov, "An S-parameter extraction technique for broad-band characterization of microstrip-to-SIW transitions," IEEE AP-S Dig., 428.4, June 2009.

[6] J.C. Rautio, "A de-embedding algorithm for electromagnetics," Int. J. Microwave Millimeter-Wave Computer-Aided Eng., vol.1, no.3, pp.282-287, 1991.

[7] H. Ito and K. Masu, "A simple through-only de-embedding method for on-wafer S-parameter measurements up to 110GHz," IEEE MTT-S International Microwave Symposium (IMS), pp. 383-386, June 2008.

[8] N. Li, K. Matsushita, N. Takayama, S. Ito, K. Okada, and A. Matsuzawa, "Evaluation of a multi-line de-embedding technique up to 110 GHz for millimeter-wave CMOS circuit design," IEICE Trans. Fundamentals, vol.E93-A, No.2, pp. 431-439, Feb. 2010.

[9] Q.-H. Bu, N. Li, K. Bunsen, H. Asada, K. Matsushita, K. Okada, and A. Matsuzawa, "Evaluation of a multi-line de-embedding technique for millimeter-wave CMOS circuit design," Asia-Pacific Microwave Conference (APMC), Yokohama, Japan, Dec. 2010.

[10] T. Hirano, K. Okada, J. Hirokawa, and M. Ando, "Thru-Line (TL) calibration technique for on-wafer measurement," Proceedings of International Symposium on Antennas and Propagation (ISAP), Paper ID: 104, Macao, November 23-26, 2010.

[11] M.A.T. Sanduleanu and J.R. Long, "CMOS integrated transceivers for 60GHz UWB communication," IEEE International Conference on Ultra-Wideband (ICUWB), pp.508-513, Singapore, September 2007.

[12] T. Hirano, H. Nakano, Y. Hirachi, J. Hirokawa, and M. Ando, "De-embedding method using an electromagnetic simulator for characterization of transistors in the millimeter-wave band," IEEE Transactions on Microwave Theory and Techniques, Vol.58, No.10, pp.2663-2672, October 2010.

[13] Mathematica, Wolfram Research, Champaign, IL [Online]. Available: http://www.wolfram.com/

[14] Ansoft HFSS. ver. 11, Ansoft, Pittsburgh, PA, 2009. [Online]. Available: http://www.ansoft.com/products/hf/hfss/

[15] Y. Ono, T. Hirano, K. Okada, J. Hirokawa, and M. Ando, "Eigenmode Analysis of Propagation Constant for a Microstrip Line with Dummy Fills on a Si CMOS Substrate," IEICE Trans. Electron., Vol.E94-C No.6, pp.1008-1015, June 2011.

[16] A.M. Mangan, S.P. Voinigescu, M.-T. Yang, and M. Tazlauanu, "De-embedding transmission line measurements for accurate modeling of IC designs," IEEE Trans. Electron Devices, vol.53, No.2, pp.235-241, Feb. 2006.

[17] T. Hirano, K. Okada, J. Hirokawa, and M. Ando, "Accuracy investigation of the de-embedding technique using open and short patterns for on-wafer RF characterization," Asia-Pacific Microwave Conference (APMC), TH3G-44, poster, pp.1436-1439, Yokohama, Japan, Dec. 2010.